

THE STRUCTURE OF COLD DARK MATTER HALOS

JOHN DUBINSKI AND R. G. CARLBERG

Department of Astronomy, University of Toronto, Toronto, Ontario, Canada M5S 1A1

Received 1990 December 26; accepted 1991 March 22

ABSTRACT

The density profiles and shapes of dark halos are studied using the results of N -body simulations of the gravitational collapse of density peaks. The simulations use from 3×10^4 to 3×10^5 particles, which allow density profiles and shapes to be well resolved. The core radius of a typical dark halo is found to be no greater than the softening radius, $\epsilon = 1.4$ kpc. The density profiles can be fitted with an analytical model with an effective power law which varies between -1 in the center to -4 at large radii. The dark halos have circular velocity curves which behave like the circular velocity contribution of the dark component of spiral galaxies inferred from rotation curve decompositions. The halos are strongly triaxial and very flat, with $\langle c/a \rangle = 0.50$ and $\langle b/a \rangle = 0.71$. There are roughly equal numbers of dark halos with oblate and prolate forms. The distribution of ellipticities in projection for dark halos reaches a maximum at $\epsilon = 0.5$, in contrast to the ellipticity distribution of elliptical galaxies, which peaks at $\epsilon = 0.2$.

Subject headings: dark matter — galaxies: structure — numerical methods

1. INTRODUCTION

In hierarchical cosmologies, dark matter halos arise from the gravitational collapse of density peaks in a random perturbation field. The process of gravitational collapse includes the merging of substructure, tidal torquing by neighboring structure, and the steady accretion of surrounding material. The result is a triaxial, slowly rotating, centrally concentrated dark halo (e.g., Efstathiou & Jones 1979; Quinn, Salmon, & Zurek 1986; Barnes & Efstathiou 1987; Frenk et al. 1988). Calculations of spherical infall in an Einstein–de Sitter universe ($\Omega = 1$) onto seed perturbations (Gunn 1977; Fillmore & Goldreich 1984; Bertschinger 1985) and onto density peaks in power-law cosmologies [$P(k) \propto k^n$] with $n < -1$ (Ryden 1988; Hoffman 1988) result in objects with characteristic power-law density profiles, $\rho \propto r^{-\alpha}$, where $1.6 \lesssim \alpha \lesssim 2.25$. These profiles are remarkably similar to the isothermal profiles ($\rho \propto r^{-2}$) derived from the observation of “flat” rotation curves in spiral galaxies (e.g., Rubin et al. 1985). The nonlinear problem has also been addressed using cosmological N -body simulations. Simulations using the cold dark matter (CDM) model (Bond & Efstathiou 1984) and power-law models succeed in producing dark halos with “flat” rotation curves in fair agreement with the spherical calculations (Frenk et al. 1985; Barnes & Efstathiou 1987; Zurek, Quinn, & Salmon 1988; Frenk et al. 1988). However, these simulations have insufficient resolution to measure density profiles and circular velocity curves of dark halos over the observable range of the rotation curves of spiral galaxies ($r \lesssim 30$ kpc). In particular, the core radii of dark halos have not been reliably ascertained in either numerical simulations or analytical calculations.

The dark halos of cosmological N -body simulations are strongly triaxial objects showing a broad variation in shapes (Frenk et al. 1988). Frenk et al. displayed the distribution of axial ratios of dark halos, although the statistical errors were fairly large. They found that there were roughly equal numbers of halos with oblate and prolate forms. The triaxial nature of dark halos has important implications for the structure of elliptical galaxies. The qualitative similarities between the

structure and kinematics of dark halos and elliptical galaxies are quite compelling. Elliptical galaxies are slowly rotating objects (Bertola & Capaccioli 1975; Illingworth 1977) supported by pressure anisotropy and are triaxial (Binney 1976). If an elliptical galaxy forms at the same time and in an analogous way to its dark halo, i.e., a dissipationless collapse, one can hypothesize that the shape of an elliptical galaxy is the same as the shape of its dark halo. We can test this hypothesis by comparing the distribution of shapes of dark halos and elliptical galaxies.

In this paper, we examine the structural properties of cold dark matter halos by measuring the core radii, the density profiles, and the distribution of shapes. We use N -body simulations containing 32,000 particles allowing sufficient resolution to quantify shapes and density profiles accurately. In § 2 we discuss the numerical methods used to simulate the formation of dark halos. In § 3 we present the density profiles and rotation curves of dark halos and compare them with observational data. We also calculate the distribution of axial ratios of dark halos and compare the ellipticity distribution of dark halos with that of elliptical galaxies. In § 4 we summarize the results and their implications. Although the dynamics of dark halos are also important in the understanding of the process of gravitational collapse and the dynamics of galaxies, we choose to defer the discussion of issues such as the rotation, velocity dispersion, and velocity anisotropy of dark halos to a subsequent paper for the sake of clarity.

2. NUMERICAL METHODS

We have developed a method for following the expansion and collapse of a dark matter halo in isolation using cosmological initial conditions and boundary conditions. Previous studies of dark halos (Frenk et al. 1988; Zurek, Quinn, & Salmon 1988; Barnes & Efstathiou 1987) used fewer particles with halos typically containing between a few hundred and a few thousand particles. Low particle resolution makes it difficult to extract structural and dynamical quantities because of the poor sampling of phase space. The effect of two-body relax-

ation is severe when N is small, especially in the dense cores of halos where the local time scales are relatively short. Two-body encounters tend to scatter particles in random directions, so that the shapes and velocity ellipsoids tend to be more isotropic than they should be. We reduce these problems by using approximately 32,000 particles in a typical peak collapse simulation. An additional simulation using approximately 280,000 particles is run for comparison to see whether the density profiles change at higher resolution.

We assign the initial positions and velocities to particles in a spherical region surrounding a density peak selected from a discrete realization of a CDM density contrast field ($H_0 = 50 \text{ km s}^{-1} \text{ Mpc}^{-1}$ and $\Omega = 1$) smoothed with a Gaussian filter with a filter length, $R_f = 0.75 \text{ Mpc}$, a scale appropriate to bright galaxies. The density field is generated in an 8 Mpc periodic cube containing 64^3 cubic mesh points. The particles in a 2 Mpc radius sphere surrounding the peak in the unfiltered density field are perturbed in position from a uniform grid according to the Zel'dovich approximation (Zel'dovich 1970) to represent the density field around the peak. The triangular cloud scheme of Hockney & Eastwood (1988) is used to solve for the Zel'dovich potential on the mesh points of the periodic cube. Peculiar velocities are assigned assuming pure growing mode perturbations and added to the local Hubble flow.

The choice of a vacuum boundary ignores some important physical effects in the evolution of the dark halo which must be taken into account. First, the vacuum boundary excludes the effect of tidal fields due to neighboring perturbations. The tidal field can be estimated and modeled in a reasonable way as described in the next section. Second, the material surrounding a density peak in an extended universe effectively retards a peak's growth and deformation during its evolution. A vacuum boundary does not include this effect, so that the spherical region as a whole which surrounds the peak will deform and collapse prematurely potentially modifying the final state. This problem is minimized by choosing a spherical region which is 3 times the filter radius used to select the peak. The majority of the substructure which conspires to form the peak is thus confined to the inner regions of the sphere, well removed from the boundary which will suffer the anomalous deformation first. We also surround the peak with a thick shell of particles containing no internal fluctuations which is perturbed self-consistently by the density fluctuations within the peak. The shell acts as a buffer between the edge of the region containing fluctuations and the vacuum, and models the retarding effect of the "rest" of the universe.

2.1. Tidal Fields

A density peak collapsing in a cosmological background is immersed in a tidal field generated by the surrounding fluctuating density field. The field induces a torque on a peak during collapse by coupling to the peak's quadrupole moment (Peebles 1969; White 1984). Since the simulations described here use isolated systems to increase the resolution, we choose to model the effect of external tidal torques on collapsing density peaks by imposing a first-order external tidal field. Internal tidal torques are generated self-consistently by the density fluctuations within the simulation sphere.

The magnitude of the external tidal field on the scale of the simulations can be estimated from the power spectrum. The first-order expansion of a tidal field due to material in a fluctuating density field outside a radius r_0 expanded about some

origin is described by the trace-free tensor

$$T_{ij}(r_0) \equiv \left. \frac{\partial^2 \Phi}{\partial x_i \partial x_j} \right|_{r=0} = -G\rho_b \int_{V(>r_0)} d^3r \frac{\delta\rho}{\rho_b}(r) \frac{(3x_i x_j - r^2 \delta_{ij})}{r^5}, \quad (1)$$

where $\delta\rho/\rho_b$ is the density contrast. The tidal acceleration due to material outside $r > r_0$ felt at the point x_j is $\sum_j T_{ij} x_j$. The dispersion in a diagonalized element of the tidal field can be calculated from the power spectrum, $P(k) = |\delta_k|^2$. The dispersion in T_{xx} , for example, is

$$\langle T_{xx}^2 \rangle(r_0) = G^2 \rho_b^2 \frac{V_u}{(2\pi)^3} \int d^3k P(k) W^2(kr_0), \quad (2)$$

where the window function is

$$W(kr_0) = \int_{V(>r_0)} d^3r e^{-ik \cdot r} \frac{3x^2 - r^2}{r^5} = 4\pi \left[\frac{\sin kr_0 - kr_0 \cos kr_0}{(kr_0)^3} \right] \quad (3)$$

and V_u is the periodic cubic volume of integration. The window function, $W(kr)$, is identical (other than the normalization) to the top-hat window function $W_{\text{th}}(kr)$ used to measure the mass fluctuation $\langle (\delta M/M)^2 \rangle$ in spheres of radius r (e.g., Peebles 1980). The dispersion in the tidal field is therefore proportional to the mass fluctuation through

$$\langle T_{xx}^2 \rangle^{1/2} = \frac{4\pi}{3} G\rho_b \left\langle \left(\frac{\delta M}{M} \right)^2 \right\rangle^{1/2}. \quad (4)$$

Similarly, one can show that $\langle T_{yy}^2 \rangle = \langle T_{xx}^2 \rangle$. In practice, T_{xx} and T_{yy} are independent Gaussian random variables. Since T_{ij} is a trace-free tensor, the value of $T_{zz} = -(T_{xx} + T_{yy})$.

The time dependence of the tidal field in the linear regime is determined by equation (4). Since $\rho_b \propto t^{-2}$ and $\delta M/M \propto t^{2/3}$ in the linear regime of the CDM model ($\Omega = 1$), the tidal field components decline as $t^{-4/3}$. In the nonlinear regime, neighboring density peaks collapse into objects which are essentially point masses. The tidal field then results from an ensemble of point masses moving apart with the general expansion of the universe, so that the tidal field components decline more rapidly as t^{-2} (e.g., Peebles 1969). For simplicity, we choose to model the tidal field using the linear regime time dependence for the duration of the simulations. Therefore, in practice we are examining the coupling of a linear regime tidal field to a fully nonlinear collapse. After the collapse of a density peak, the tidal torque drops rapidly, since the moment arm represented by the radius of the initially expanding region which the tidal field pushes against to produce the torque stops growing at the turnaround time (Barnes & Efstathiou 1987; Ryden 1987). The overestimate of the strength of the tidal field arising from the use of the linear time dependence into the nonlinear regime should have a minor influence on the total amount of angular momentum transferred to the peak, since collapse and thus decoupling occur approximately at the time when the field enters the nonlinear regime. Tidal coupling to a nearby virialized neighbor at late times after the collapse may also transfer angular momentum, but simulations show that the bulk of the angular momentum is acquired prior to collapse (Barnes & Efstathiou 1987).

The tidal field is modeled in the simulations using a tidal tensor with principal components $T_{xx} = 2f_t \sigma_t$, $T_{yy} = -f_t \sigma_t$, and $T_{zz} = -f_t \sigma_t$, where $\sigma_t \equiv \langle T_{xx}^2 \rangle^{1/2}$ and f_t is the number of deviations. We have chosen a value of $f_t \approx 1$ for all of the simulations. This tidal field is oriented randomly with respect to the principal axes of the density peak. In a cosmological setting, however, the orientation of tidal fields should be weakly correlated with the orientation of density peaks. We checked for this effect by measuring the distributions of the cosine angles of the initial torque with respect to the principal axes of the perturbation for 30 density peaks in a 128^3 mesh representation in a 16 Mpc box. These distributions were compared with the similar distributions measured assuming the tidal fields were oriented randomly. The two distributions are very similar, indicating that the choice of random orientations is a reasonable first approximation. The tidal acceleration is calculated at each time step and added to the acceleration due to internal gravitational forces. The validity of this method is tested by examining the rate of angular momentum growth and calculating the dimensionless spin parameter, $\lambda \equiv J|E|^{1/2}G^{-1}M^{-5/2}$, of the halos after the simulations. In the linear regime, the angular momentum is observed to grow at a rate proportional to t as expected. We find that $\lambda = 0.041 \pm 0.024$, consistent with numerical values found by other studies (e.g., Barnes & Efstathiou 1987).

2.2. Simulation Parameters

A total of 14 peak collapses were simulated with peak heights in the range of 1.5σ to 3.4σ , with a mean value of 2.4σ . The peaks were chosen randomly from different realizations of the density contrast in an 8 Mpc box. The peaks were found by smoothing the density contrast field with a Gaussian filter of radius $R_f = 0.75$ Mpc, corresponding to a filter mass of $M_f = 4.6 \times 10^{11} M_\odot$. All of the simulations used approximately 33,000 particles in a sphere of radius 2.3 comoving Mpc. The number of particles varied in different simulations, since the spherical boundaries were chosen after the particles were perturbed from the grid. The typical particle mass was $1.2 \times 10^8 M_\odot$. The CDM spectrum (Bond & Efstathiou 1984) was normalized to the value of the J_3 integral of $277h^{-3} \text{Mpc}^3$ measured for galaxies on a scale of $10h^{-1} \text{Mpc}$ (Davis & Peebles 1983) assuming that the Hubble constant H_0 is $50 \text{ km s}^{-1} \text{ Mpc}^{-1}$, so that $h = \frac{1}{2}$. The bias parameter b was assumed to be unity.

Once positions and velocities were assigned to the particles, each model was evolved under its self-gravity with an N -body tree code modified to incorporate the influence of a tidal field (Barnes & Hut 1986; Dubinski 1988). We used a tolerance parameter $\theta = 1.0$, and all cell-particle forces were calculated to quadrupole order. The softening radius, ϵ , was 1.4 kpc. All simulations were started at $z_0 = 42.2$ and finished at $z_f \approx 1.0$ ($z_f = 0$ for $b = 2$), at which time the halos were virialized (Fig. 1). The simulations were not run any further, since the objects were not evolving significantly at this time.

3. THE STRUCTURE OF DARK HALOS

3.1. Measuring Shapes and Density Profiles

The shape of an ellipsoidal mass distribution is defined through the axial ratios of the density surface contours. With the assumption that the density distribution is stratified in similar ellipsoids, it is possible to determine the axial ratios without knowledge of the radial density distribution. The

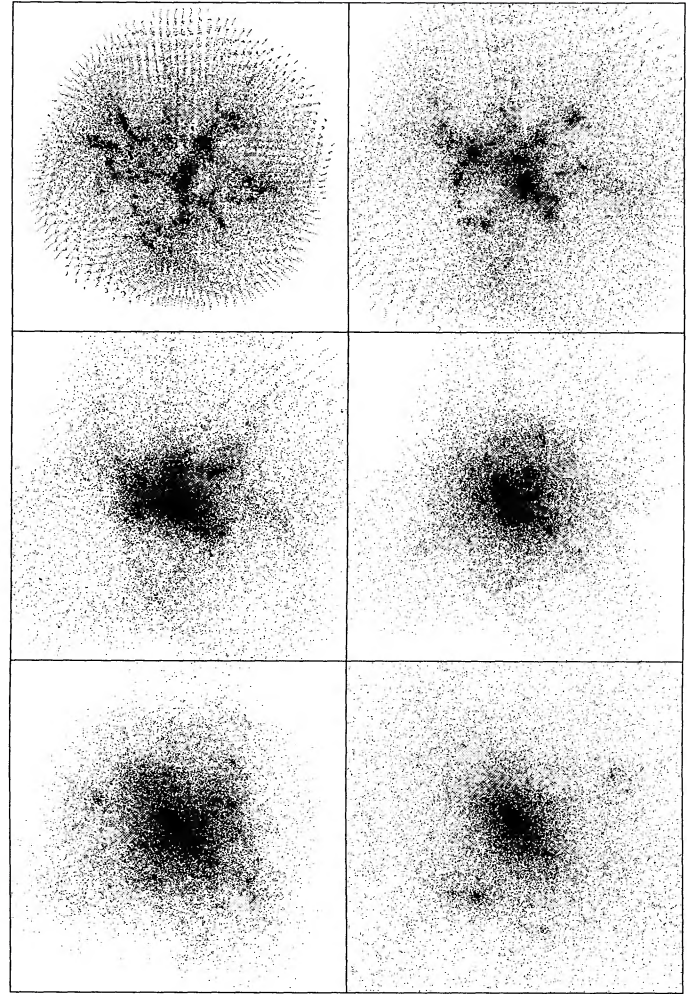


FIG. 1.—Time evolution of the formation of a dark halo from the collapse of a density peak. The panels viewed from left to right and down represent the state of the collapse at $z = 7.7, 4.7, 3.4, 2.6, 2.1, 1.0$ with $b = 1$. The boxes are all 430 kpc wide. The strongly inhomogeneous collapse of the density peak leads to the formation of a centrally concentrated, triaxial dark halo.

density of an ellipsoidal distribution is

$$\rho \equiv \rho(a) \quad \text{with} \quad a = \left(x^2 + \frac{y^2}{q^2} + \frac{z^2}{s^2} \right)^{1/2}, \quad (5)$$

where a is the elliptical radius and q and s are the axial ratios with $s \leq q \leq 1$. It is simple to show that the axial ratios can be derived from the tensor

$$M_{ij} = \sum \frac{x_i x_j}{a^2} \quad (6)$$

through

$$q = \left(\frac{M_{yy}}{M_{xx}} \right)^{1/2} \quad \text{and} \quad s = \left(\frac{M_{zz}}{M_{xx}} \right)^{1/2}, \quad (7)$$

where M_{xx} , M_{yy} , and M_{zz} are the principal components of the tensor, with $M_{zz} \leq M_{yy} \leq M_{xx}$. This scheme has the advantage that there is an equal weight for each particle in the tensor, independent of radius. With the large number of particles in the dark halos presented here, accurate axial ratios can be determined.

In practice, the value of the elliptical radius a in M_{ij} for a given particle is not known in advance, since it depends on q and s (the quantities we are hoping to determine) through equation (5). The axial ratios are therefore determined using an iterative procedure. On the first pass, M_{ij} is calculated assuming that the contours are spherical, so that $q = s = 1$ and $a = r$. The particle positions are first rotated into the diagonalized frame of M_{ij} . The values of q and s determined from M_{ij} are then used to recalculate a in this new frame and fed back into the M_{ij} relation to determine new values of q and s . When the input values match the output values within a certain tolerance, convergence to the true axial ratios is achieved (see also Katz 1991).

The accuracy of the method was tested by measuring the axial ratios in a particle realization of the density distribution $\rho \propto a^{-2}$ with different values of q and s . Axial ratios determined from distributions containing 250, 1000, and 5000 particles have random errors of about 10%, 4%, and 2%, respectively, scattered about the true axial ratio values, provided that $q, s \lesssim 0.8$. For more spherical distributions with $q, s \gtrsim 0.8$, there is a bias toward underestimating the axial ratios. Measurements of spherical distributions ($q = s = 1$) of 250, 1000, and 5000 particles gave mean values of s of 0.8, 0.9, and 0.95, respectively, with q slightly larger and similar percentage errors to those above.

Dark halos are generally not perfect ellipsoids; rather, they exhibit a definite gradient in the axial ratio profiles. We have chosen to measure representative axial ratios instead of the profiles by using all particles within ellipsoidal volumes with elliptical radii of 25, 50, and 100 kpc. The axial ratios measured this way represent a “mean” value within the volume. Density profiles are then determined by counting particles in ellipsoidal shells of the fixed axial ratios calculated using the 100 kpc radius ellipsoidal volume.

3.2. Density Profiles

A convenient and remarkably good fit to the density profiles (Fig. 2) of the dark halos is Hernquist’s (1990) density distribution modified for an ellipsoidal system,

$$\rho(r) = \frac{M_s a_s}{2\pi q s} \frac{1}{r(r + a_s)^3}, \quad (8)$$

where we identify r with the elliptical radius a , and $q = b/a$ and $s = c/a$ are the axial ratios of the halo. The axial ratios are calculated as described above. We fit the model with two free parameters: the effective mass, M_s , and the scaling radius, a_s . We use a nonlinear least-squares method with equal weighting for each point to determine the fits. Since the axial ratios are different for various models, we compare the geometric mean of the scaling radius, $r_s = (a_s^3 q s)^{1/3}$, instead of the scaling radius directly. The mean scaling radius of the fits is $\langle r_s \rangle = 10^{1.43 \pm 0.07}$ kpc, while the mean effective mass is $M_s = 10^{12.33 \pm 0.23} M_\odot$. In the spherical top-hat model, the density contrast of a mass shell at the time of virialization is $\rho/\rho_c \approx 18\pi^2 \approx 177$. If we define the virialized “edge” of a dark halo at this density surface ($\rho/\rho_c \geq 125$ in these measurements), we find a mean halo mass $M_{\text{halo}} = 10^{12.18 \pm 0.22} M_\odot$. Even though the effective mass is a fitting parameter, it agrees well with the “virialized” mass of the halos.

Figure 2 shows the least-squares fit of a Hernquist profile to the dark halo density profiles. Each set of data points has

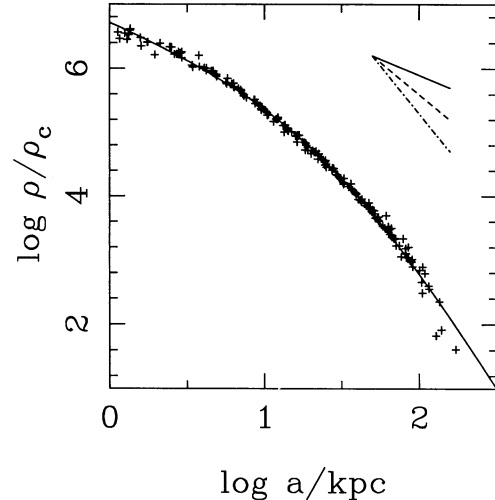


FIG. 2.—Density profiles of dark halos. Density is in units of the critical density ρ_c , and the elliptical radius a is in kpc. Thirteen points were used for the two-parameter fit of Hernquist’s profile for each of the 14 halos. Each set of points has been renormalized to the fiducial Hernquist profile, with $r_s = 28$ kpc and $M_s = 2.1 \times 10^{12} M_\odot$ represented by the solid line. The lines in the upper right-hand corner present power-law slopes of -1 , -2 , and -3 , respectively.

been renormalized to the fiducial Hernquist profile of the mean mass and scaling radius of the simulations. The fit is very good, with a dispersion in $\log \rho$ of 0.09. The density profiles are slightly shallower than the Hernquist profile in the center of the halos, though the density is still increasing fairly steeply at the softening radius equal to 1.4 kpc. We conclude that the core radii of dark halos are effectively zero. The density profiles are not simply described by a unique power law as predicted by spherical infall models. Rather, the power law varies from about -1 in the center to about -4 at large radii. The behavior at large radii in the simulations is dubious because of the use of approximate boundary conditions. However, the trend for a steepening power law at intermediate radii is still apparent. The effective power law for the models is approximately -3 at 60 kpc, well within the virialized “edge” ($\rho/\rho_c \geq 125$) of the halos at approximately 150 kpc. The central behavior of the simulations may be modified by two-body relaxation effects. We tested for these effects using an additional simulation containing $\approx 280,000$ particles and using the same initial conditions as a small simulation. Figure 3 reveals that the density profiles are virtually identical in the center to the softening radius, suggesting that relaxation effects are negligible.

The differences between the density profiles of the dark halos and the profiles of spherical infall models are probably due to the effects of tidal torques. The tangential accelerations induced by tidal fields place particles on nonradial orbits, increasing the isotropy of the velocity ellipsoid. Isotropic systems permit shallower density profiles than radial systems. For example, spherical systems with power-law density profiles, $\rho \propto r^{-\alpha}$, in hydrostatic equilibrium have a radial velocity dispersion profile given by

$$\sigma_r^2(r) = \frac{\sigma_{r0}^2}{(3 - \alpha)(\alpha - \beta - 1)} \left(\frac{r}{r_0}\right)^{2-\alpha}, \quad (9)$$

where $\beta = 1 - \sigma_t^2/\sigma_r^2$ is the anisotropy parameter with $\beta = 0$ for isotropic orbits and $\beta = 1$ for purely radial orbits (e.g., Ryden 1991). The only permitted solutions are those with

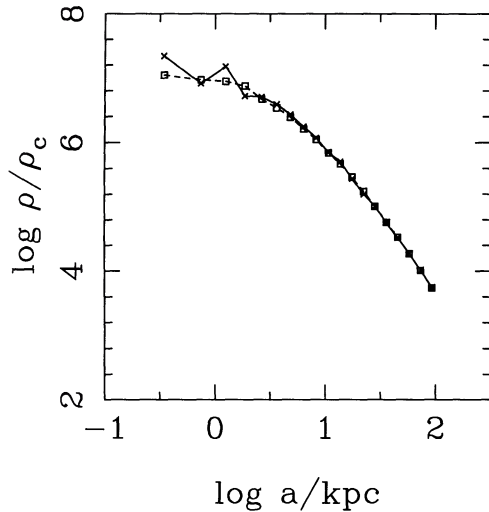


FIG. 3.—Density profiles of the 32,000 and 280,000 particle simulations. The same density contrast field is used to generate initial conditions. The squares joined by the dashed line follow the density profile of the large simulation. The crosses joined by the solid line follow the density profile of the small simulation. The profiles are virtually identical to within the softening radius of 1.4 kpc, where they level off, and Poisson noise due to a lack of particles begins to dominate in the smaller simulation.

$1 + \beta < \alpha < 3$. Spherical infall models with purely radial orbits ($\beta = 1$) (e.g., Fillmore & Goldreich 1984) are constrained to density profiles steeper than r^{-2} . However, if the orbits are isotropic, then density profiles as shallow as r^{-1} are permitted. We are currently investigating the kinematics of the dark halos, which will be discussed in full in a subsequent paper. Preliminary results show that $\beta \lesssim 0.2$ in the center of the dark halos, supporting the claim that shallow central density profiles require a nearly isotropic velocity ellipsoid. Ryden (1988) also obtained a shallower density profile ($\alpha = 1.6$) in her analytical calculations of peak collapse when incorporating the influence of tidal torques. Another fundamental assumption in spherical infall models is that radial orbits are self-similar (e.g., Fillmore & Goldreich 1984). This assumption eliminates a scale for the problem, so that power-law density profiles must arise a priori. The action of selecting a density peak of a certain scale (i.e., the filter radius) breaks the self-similar assumption, so there is no reason to believe that the density profile should follow an exact power law. The scale of the simulation is finally characterized by the scaling radius of the Hernquist density profile.

Hernquist's profile was motivated by the desire for a simple analytic potential-density pair to account for the de Vaucouleurs luminosity profile of elliptical galaxies. The surface density profile of Hernquist's function resembles a de Vaucouleurs profile with effective radius $R_e = 1.8r_s$ (Hernquist 1990), suggesting the naive interpretation that elliptical galaxies and dark halos are one and the same. However, the resemblance of dark halos to elliptical galaxies in this case is only circumstantial. The effective radius for dark halos is $R_c = 50$ kpc, a factor of 8 larger than the observed value for bright elliptical galaxies of 6 kpc ($h = \frac{1}{2}$) (Kormendy 1977). At first glance, the Hernquist profile of dark halos seems to contradict the standard isothermal picture of dark halos. However, the effective power law of the profile varies from -1 to -2.5 within the scaling radius of the model. The resulting rotation curves should

therefore appear fairly constant, at least out to the scaling radius.

Figure 4 presents the circular velocity curves of the dark halos. The mass was binned in spherical shells of roughly equal mass to estimate the circular velocity, $v_c(r) = [GM(r)/r]^{1/2}$. The second-order effects of the flattened potential have been ignored for simplicity. All of the curves have been renormalized to the fiducial Hernquist profile described above. The rotation curves of the simulations are fairly constant in the range 10–60 kpc, consistent with expectations of the Hernquist profile, though there is a tendency for them to decline. Figure 5 presents the rotation curve of the dark halo resulting from the 280,000 particle simulation. Also shown is the rotation curve derived from the Hernquist profile fit to the density profile with $M_s = 2.4 \times 10^{12} M_\odot$ and $r_s = 29$ kpc. The Hernquist profile rotation curve is given by

$$v_c(r) = \frac{(GM_s r)^{1/2}}{r + r_s}, \quad (10)$$

reaching a maximum at $r = r_s$. The model rotation curve overestimates the rotation at large radii, reflecting the tendency for the Hernquist profile to overestimate the density in the center. However, the agreement is fairly good. We turn the problem around by fitting a Hernquist rotation curve to the data to derive the mass and the scaling radius. This fit gives the parameters $M_s = 2.0 \times 10^{12} M_\odot$ and $r_s = 26$ kpc, which compare well with the values derived from the density profiles.

The dark halo rotation curves are in reasonable agreement with observations of rotation in spiral galaxies. We fitted the Hernquist model rotation curve to the data for NGC 3198 (van Albada et al. 1985) and determined the parameters $r_s = 12.2$ kpc and $M_s = 2.7 \times 10^{11} M_\odot$ assuming that the dark halo dominates (Fig. 6). The curve is particularly successful at fitting the inner regions of the rotation curve, though it may decline more rapidly than an extrapolation of the data would suggest. However, the fit is as good as those determined with isother-

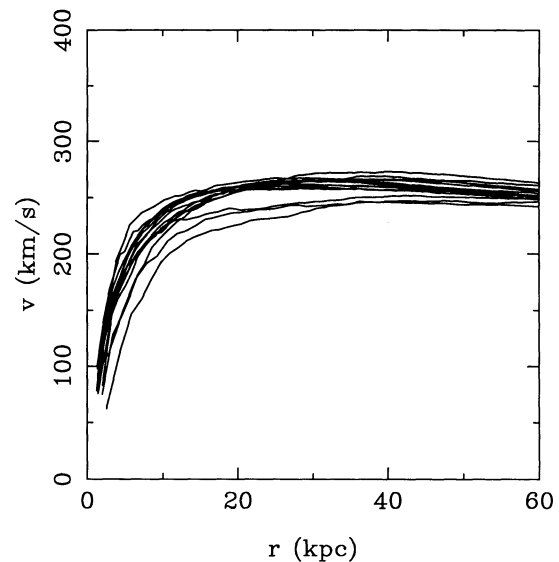


FIG. 4.—Rotation curves of the dark halos. Each curve has been renormalized according to the density profile fit to the fiducial spherical Hernquist profile, with $r_s = 28$ kpc, $M_s = 2.1 \times 10^{12} M_\odot$, and $v_{\max} = 290$ km s $^{-1}$. The curves are fairly constant between 10 and 60 kpc, though they do decline slightly.

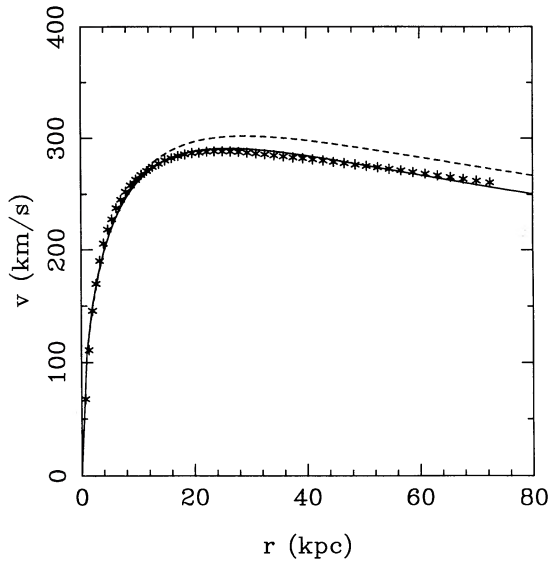


FIG. 5.—Rotation curve of the 280,000 particle simulation. The asterisks are the points measured from the dark halo. The dashed line is the rotation curve derived from the Hernquist profile fit to the density profile, with $r_s = 29$ kpc and $M_s = 2.4 \times 10^{12} M_\odot$. Note that the curve overestimates the rotation velocity at large radii, showing that the Hernquist profile slightly overestimates the density in the center. The solid line is the fit of a Hernquist rotation curve to the data. The scaling radius and effective mass of this fit are $r_s = 26$ kpc and $M_s = 2.0 \times 10^{12} M_\odot$, in reasonable agreement with the density profile fit.

mal models of dark halos with $\rho \propto (r^2 + a^2)^{-1}$ (e.g., Kent 1987).

Hernquist's profile succeeds in fitting the dark halos, since it is coreless ($\rho \propto r^{-1}$ in the center), and the effective power law declines monotonically with radius. The theoretical rotation curve is also fairly constant in the range $r_s/2 < r < 2r_s$. The scaling of the CDM model makes this range compatible with the observations of rotation curves in spiral galaxies. However, the success of Hernquist's profile at modeling dark halos should be viewed with some caution. The density profiles were

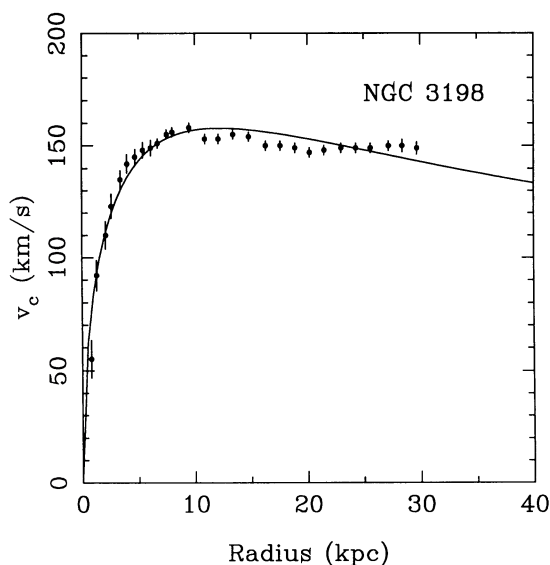


FIG. 6.—Best-fit Hernquist rotation curve to the NGC 3198 data assuming the dark matter halo dominates. The scaling radius is $r_s = 12.2$ kpc, and the mass is $M_s = 2.7 \times 10^{11} M_\odot$.

TABLE 1
RADIAL DEPENDENCE OF THE MEAN AXIAL RATIOS

a (kpc)	b/a	c/a
25.....	0.56 ± 0.12	0.42 ± 0.06
50.....	0.64 ± 0.14	0.45 ± 0.08
100.....	0.71 ± 0.13	0.50 ± 0.09

only fitted out to the radius which contained roughly 60% of the mass determined in the fit, $3.5r_s$. The total mass, M_s , of the halo in the model should be interpreted as a fitting parameter only and not necessarily the true mass of the halo. Also, the density profile may drop off too rapidly at large radii because of truncation caused by an artificially high tidal field or a lack of secondary infall due to the vacuum boundary. For this reason, a conservative estimate of the radius where the fit is reliable is about $2r_s$.

3.3. Shapes of Dark Halos

The axial ratios of each dark halo are determined with the tensor method described above, using all particles within three ellipsoidal volumes with semimajor axes of 25, 50, and 100 kpc. A range of radii is chosen to test for spurious effects introduced by a radial gradient in the axial ratios. Depending on the degree of central concentration and the semimajor axis, between 2000 and 30,000 particles are used for the halo shape determination.

The dark halos are very flat, triaxial objects, as shown by the mean values of their axial ratios at different radii (Table 1). There is also a tendency for the halos to be rounder at larger radii, as shown by the systematic increase in the mean axial ratios with larger radius. Figure 7 displays the distribution of axial ratios. The central regions of halos ($\lesssim 25$ kpc) are generally more prolate than oblate, with 12 of 14 halos having $c/$

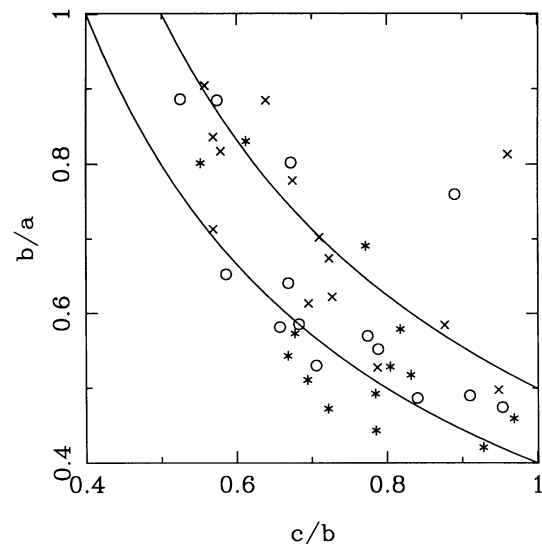


FIG. 7.—Distribution of axial ratios for the dark halos. Axial ratios measured from particles within 25 kpc (asterisks), 50 kpc (circles), and 100 kpc (crosses) are displayed. The solid lines represent ellipsoids with $c/a = 0.4$ and 0.5 . Note that the inner regions (< 25 kpc) of the halos are very flat and prolate as shown by the cluster of stars in the lower right-hand corner. The shapes measured at larger radii represent oblate and prolate forms in approximately equal numbers.

$b > b/a$. Measurements using a large radius (100 kpc) reveal no strong preference for either oblate or prolate types, with 6 of 14 halos having $c/b > b/a$. The extreme flattening of the halos is purely the result of pressure anisotropy, with rotation having a negligible effect, as shown by the mean value of $\lambda = 0.041$. The degree of velocity anisotropy will be discussed in a subsequent paper on the dynamics.

It is interesting to compare these results with those of other authors (Frenk et al. 1988; Warren et al. 1990). Frenk et al. found that halos are *rounder* in the inner regions than the outer regions, opposite to the conclusions of this study. Our distribution of intrinsic shapes is similar at large radii (i.e., roughly equal numbers of prolate and oblate shapes), though the halos are flatter than their results. The axial ratio c/a for most of the halos appears to settle to a value between 0.4 and 0.5 regardless of the intrinsic shape (Fig. 7). Perhaps two-body relaxation effects are acting to give rounder dark halos in the Frenk et al. simulations, since these halos only contain a few hundred particles. The axial ratios of the 140 dark halos in Warren et al.'s (1990) simulation are also considerably rounder. Warren et al. used a different method to determine the axial ratios, and this may be the source of the different axial ratio distribution. Monte Carlo testing shows that the random errors in the axial ratios using our technique are generally less than 5% as discussed in § 3.1, and are unlikely to account for the difference. In summary, we believe we have accurately simulated and measured the shapes of CDM halos, the greater accuracy being a consequence of larger N , realistic cosmological boundary conditions, and a robust measurement technique.

Elliptical galaxies are believed to be triaxial bodies (Binney 1976) supported by pressure anisotropy not unlike the dark halos of this study. Although dark halos and elliptical galaxies have different density profiles as seen above, it is still instructive to compare their shapes. If elliptical galaxies form dissipationlessly (e.g., van Albada 1982; Aguilar & Merritt 1990) in the center of dark halos *ab initio*, they may have the same shape distribution as the dark halos. We can examine this hypothesis by comparing the distribution of projected axial ratios of elliptical galaxies to that of dark halos.

The probability distribution function of projected axial ratios is given by

$$P(q_a) = \iint f(q, s) P(q_a | q, s) dq ds, \quad (11)$$

where $P(q_a | q, s)$ is the conditional probability distribution function of the projected (apparent) axial ratio q_a given the true axial ratios q and s (Binney 1985), under the assumption that the density surfaces are similar ellipsoids and $f(q, s)$ is the intrinsic distribution of shapes. Since the sample of dark matter halos is assumed to be random, we can approximate $P(q_a)$ using

$$P(q_a) = \frac{1}{n} \sum_{i=1}^n P(q_a | q_i, s_i). \quad (12)$$

Figure 8 shows the distribution of ellipticities, $\epsilon = 1 - q_a$, for the halos using the axial ratios measured at 25, 50, and 100 kpc, along with the renormalized frequency histogram of ellipticities of elliptical galaxies (Binney & de Vaucouleurs 1981). The ellipticity distribution of the dark halos peaks sharply at $\epsilon = 0.5$ and lacks round objects, in stark contrast to the ellipticity distribution of elliptical galaxies which peaks at $\epsilon = 0$ and drops to zero at $\epsilon = 0.6$. The distributions of Benacchio &

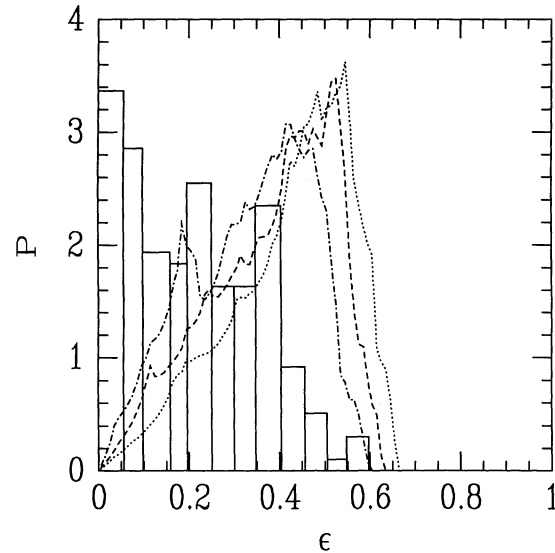


FIG. 8.—Probability distribution of ellipticities for elliptical galaxies and dark halos. The histogram is the renormalized data by Binney & de Vaucouleurs (1981). The three curves are the probability distributions derived from axial ratios measured out to 25 kpc (dotted line), 50 kpc (dashed line) and 100 kpc (dashed-dot line) from the center of the dark halos. Note that the elliptical galaxies are considerably rounder than the dark halos.

Galetta (1980) and Djorgovski (1986) have fewer round objects, with the distribution peaking at $\epsilon = 0.2$. Nevertheless, a comparison of the distributions reveals that dark halos are much flatter than elliptical galaxies. A projection of axial ratios found from Couchman's (1991) data analyzed with our shape algorithm produce ellipticity distributions remarkably similar to those presented in Figure 8. Both distributions rise steadily to $\epsilon = 0.5$ and drop off rapidly at $\epsilon = 0.6$. Very flattened virialized structures apparently arise generically in simulations of the collapse of Gaussian density peaks despite different choices of the power spectrum.

Although the shapes of elliptical galaxies are in strong discord with the shapes of dark halos, objects which were more likely to form in a purely dissipationless collapse are in better agreement. The ellipticity distributions of nonnucleated dwarf ellipticals peak at $\epsilon = 0.4$ and have a much larger fraction of flattened objects in comparison with those of bright ellipticals (Ferguson & Sandage 1989). West, Dekel, & Oemler (1989) estimated the ellipticities of a sample of 55 rich clusters and discovered that the ellipticity distribution of clusters also peaks at $\epsilon \approx 0.4$ and reveals a paucity of rounder objects.

4. CONCLUSIONS

We draw the following conclusions from our analysis of the density profiles and shapes of dark halos:

1. The core radii of these CDM dark halos are no greater than the softening radius of the simulations.
2. Hernquist's density distribution is a good description of the density profile of dark halos out to approximately 2 scaling radii.
3. The circular velocity curves of CDM dark halos agree with the inferred dark halo contribution to rotation curves in spiral galaxies over the observed range of radii ($r \lesssim 30$ kpc).
4. Dark halos are very flat, with $\langle c/a \rangle = 0.50$. The central regions of dark halos ($r \lesssim 25$ kpc) are flatter than the outer regions. The shapes of the central regions are predominantly

prolate, while the shapes of the outer regions are divided equally between prolate and oblate forms. By implication, very flat dissipationless structures arise in the collapse of density peaks in hierarchical Gaussian random fields of perturbations derived from a power spectrum with a power index $n \approx -2$.

5. Elliptical galaxies are much rounder than dark halos, as shown by a comparison of apparent ellipticities, suggesting that simple dissipationless pictures of elliptical galaxy forma-

tion fail in the CDM model, or more generally in hierarchical models with $n \approx -2$.

We thank Konrad Kuijken, Barbara Ryden, and the referee, Bernard Jones, for useful comments. We also thank Hugh Couchman for providing his data for shape analysis. We gratefully acknowledge a grant from the Pittsburgh Supercomputing Center and support from NSERC of Canada.

REFERENCES

- Aguilar, L. A., & Merritt, D. 1990, *ApJ*, 354, 33
 Barnes, J., & Efstathiou, G. 1987, *ApJ*, 319, 575
 Barnes, J., & Hut, P. 1986, *Nature*, 324, 446
 Benacchio, L., & Galetta, G. 1980, *MNRAS*, 193, 885
 Bertola, F., & Capaccioli, M. 1975, *ApJ*, 200, 439
 Bertschinger, E. 1985, *ApJS*, 58, 39
 Binney, J. 1976, *MNRAS*, 177, 19
 ———. 1985, *MNRAS*, 212, 767
 Binney, J., & de Vaucouleurs, G. 1981, *MNRAS*, 194, 679
 Bond, J. R., & Efstathiou, G. 1984, *ApJ*, 285, L45
 Couchman, H. M. P. 1991, private communication
 Davis, M., & Peebles, P. J. E. 1983, *ApJ*, 267, 465
 Djorgovski, S. 1986, Ph.D. thesis, Univ. of California, Berkeley
 Dubinski, J. 1988, M.Sc. thesis, Univ. of Toronto, Toronto
 Efstathiou, G., & Jones, B. J. T. 1979, *MNRAS*, 186, 133
 Ferguson, H. C., & Sandage, A. 1989, *ApJ*, 346, L53
 Fillmore, J. A., & Goldreich, P. 1984, *ApJ*, 281, 1
 Frenk, C. S., White, S. D. M., Davis, M., & Efstathiou, G. 1988, *ApJ*, 327, 507
 Frenk, C. S., White, S. D. M., Efstathiou, G., & Davis, M. 1985, *Nature*, 317, 595
 Gunn, J. 1977, *ApJ*, 218, 592
 Hernquist, L. 1990, *ApJ*, 356, 359
 Hockney, R. W., & Eastwood, J. W. 1988, *Computer Simulation Using Particles* (Bristol: Arrowsmith)
- Hoffman, Y. 1988, *ApJ*, 328, 489
 Illingworth, G. 1977, *ApJ*, 218, L43
 Katz, N. 1991, *ApJ*, 368, 325
 Kent, S. 1987, *AJ*, 93, 816
 Kormendy, J. 1977, *ApJ*, 218, 333
 Peebles, P. J. E. 1969, *ApJ*, 155, 393
 ———. 1980, *The Large-Scale Structure of the Universe* (Princeton: Princeton Univ. Press)
 Quinn, P. J., Salmon, J. K., & Zurek, W. H. 1986, *Nature*, 322, 329
 Rubin, V. C., Burstein, D., Ford, W. K., & Thonnard, N. 1985, *ApJ*, 289, 81
 Ryden, B. S. 1987, Ph.D. thesis, Princeton Univ.
 ———. 1988, *ApJ*, 333, 78
 ———. 1991, *ApJ*, 370, 15
 van Albada, T. S. 1982, *MNRAS*, 201, 939
 van Albada, T. S., Bahcall, J. N., Bergeman, K., & Sancisi, R. 1985, *ApJ*, 295, 305
 Warren, M. S., Zurek, W. H., Quinn, P. J., & Salmon, J. K. 1990, preprint
 West, M. J., Dekel, A., & Oemler, A., Jr. 1989, *ApJ*, 336, 46
 White, S. D. M. 1984, *ApJ*, 286, 38
 Zel'dovich, Ya. B. 1970, *AA*, 5, 84
 Zurek, W. H., Quinn, P. J., & Salmon, J. K. 1988, *ApJ*, 330, 519